Towards the use of bioresorbable fibers in time-domain diffuse optics

Laura Di Sieno[1], Nadia G. Boetti[2], Alberto Dalla Mora[1,*], Diego Pugliese[3], Andrea Farina[4], Sanathana Konugolu Venkata Sekar[1], Edoardo Ceci-Ginistrelli[3], Davide Janner[3], Antonio Pifferi[1,4], Daniel Milanese[3,5]

[1] Politecnico di Milano, Dipartimento di Fisica, Piazza Leonardo da Vinci 32, 20133 Milano, Italy
[2] Istituto Superiore Mario Boella, Via P. C. Boggio 61, 10138 Torino, Italy
[3] Politecnico di Torino, Dipartimento di Scienza Applicata e Tecnologia and INSTM research unit, Corso Duca degli Abruzzi 24, 10129 Torino, Italy
[4] Consiglio Nazionale delle Ricerche, Istituto di Fotonica e Nanotecnologie, Piazza Leonardo da Vinci 32, 20133 Milano, Italy
[5] Consiglio Nazionale delle Ricerche, Istituto di Fotonica e Nanotecnologie, Via alla Cascata, 56/C, 38123 Trento, Italy

In the last years bioresorbable materials are gaining increasing interest for building implantable optical components for medical devices. In this work we show the fabrication of bioresorbable optical fibers designed for diffuse optics applications, featuring large core diameter (up to 200 µm) and numerical aperture (0.17) to maximize the collection efficiency of diffused light. We demonstrate the suitability of bioresorbable fibers for time-domain diffuse optical spectroscopy firstly checking the intrinsic performances of the setup by acquiring the instrument response function. We then validate on phantoms the use of bioresorbable fibers by applying the MEDPHOT protocol to assess the performance of the system in measuring optical properties (namely, absorption and scattering coefficients) of homogeneous media. Further, we show an ex-vivo validation on a chicken breast by measuring the absorption and scattering spectra in the 500-1100 nm range using interstitially inserted bioresorbable fibers. This work represents a step toward a new way to look inside the body using optical fibers that can be implanted in patients. These fibers could be useful either for diagnostic (e.g. for monitoring the evolution after surgical interventions) or treatment (e.g. photodynamic therapy) purposes.
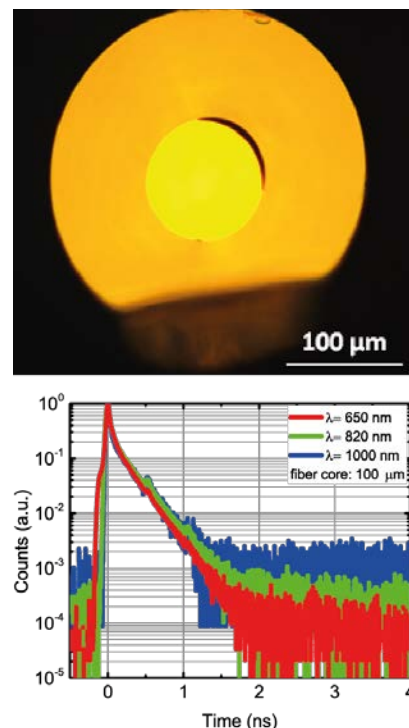
Microscopy image of the 100 µm core bioresorbable fiber (top) and the instrument response function acquired with a diffuse optics system close to the state-of-the-art based on the same fiber (bottom).

1. Introduction

Bioresorbability is intended as the ability of a material to be destroyed by the human body without leaving any harmful residual, minimizing the tissue reactions or enhancing a positive response, such as stimulating tissue regeneration. Bioresorbable materials are of high interest and have been studied in the past decades to be exploited for different applications, as they eliminate the need for follow-up explant surgery. Some of them, such as resorbable stitches, are commonly employed in everyday surgical procedures. The possibility to leave a device in place after its function is completed, without the need for retrieval, expands the range of applicability of optical tools in clinics and further diminishes the impact of minimally invasive methods.

Bioresorbable materials are gaining interest also for fabricating optical components to be used in therapy, monitoring and diagnostics [1,2]. Several bioresorbable optical components have been developed, such as microlens arrays [2], diffraction gratings [3], reflective plates [1], photonic crystals [4], waveguides [5,6] and optical fibers [7,8].

In terms of materials suitable for bioresorbable optics, Dupuis *et al.* published the first biodegradable optical fiber based on a cellulose multilayer structure [7]. More recently, extensive research was performed on silk-based materials [1,9] and hydrogels [2]. Spider silks, in particular, are specifically effective for implantable sensing devices [1], while hydrogels are studied for applications in Optogenetics, cellular scaffolding [10] or photochemical tissue bonding [6]. Synthetic polymers, such as poly(L-lactic acid) (PLA), commonly used for conventional implantable devices like resorbable sutures, have been demonstrated in waveguides for increased depth penetration for light delivery and retrieval [6].

Calcium Phosphate Glasses (CPGs) are widely studied materials for applications in hard and soft tissue engineering, and their resorbability and biocompatibility have been proved both in-vivo and in-vitro [11,12]. A recent work by some of us proposed the employment of CPG as a new material for bioresorbable optical components [13]. They present a good biocompatibility without encountering the batch-to-batch variability that is typical of some biologically derived materials. Enhancing and characterizing the optical properties of opportune compositions of CPGs allowed overcoming some of the limitations of polymers, such as high attenuation and poor transparency in the blue and near UV region [13]. Using CPGs, the feasibility of bioresorbable optical fibers was previously demonstrated, with attenuation loss coefficients of 1.9 and 4.7 dB m^{-1}, at 1300 and 633 nm, respectively, that are 1 to 2 orders of magnitude lower as compared to what reported so far for bioresorbable waveguides [7,8,10,14,15].

The availability of bioresorbable fibers can open new perspectives in clinical applications. Fibers could be inserted during interventions and left in place to monitor the healing process or detect inflammation or abnormal response. Also, they could be used to track the regeneration of tissues in implants with no burden since the fiber is entrenched by the tissue and then reabsorbed. In the brain, they may be employed to monitor deep hypoxia or hemorrhage in the sub-acute phase after brain injury [16]. Finally, they could be applied also for interstitial photodynamic and photothermal therapies with in-situ irradiation [17,18]. In general, the bioresorbability lessens the impact of inserted optical fibers and thus extends their possible adoption in clinical practice also for more routine interventions.

To move a step forward in this direction, we need to find out which information can be potentially carried by optical fibers and whether the fibers we propose are suitable for the purpose. The aim of the present work is to explore the aptness of CPG fibers to perform time-domain broadband diffuse optical spectroscopy (TD-DOS) deep into biological tissues. Since TD-DOS can provide absolute estimate of the absorption and reduced scattering spectra of the diffusive medium [19,20], it conveys information on the chemical composition (mainly water, oxy- and deoxy-hemoglobin, water, lipids, collagen), on the functional status (e.g. oxygenation) and on the scattering properties (changes in tissue microstructure, edema) [21]. Such information can then be related to the tissue regeneration, to the healing process or to a harmful evolution.

To assess the aptness of the new bioresorbable fibers for TD-DOS we have followed shared protocols devised at the international level during the last ten years for the objective performance assessment of diffuse optics instruments. In particular, we have used the analysis of the Instrument Response Function (IRF), as described in the Basic Instrumental Performance (BIP) protocol [22] for the characterization of the basic instrument performances independent from the medium under study. Then, we have applied the linearity test contained in the MEDPHOT protocol [23] to ascertain the performance of the bioresorbable fiber system in retrieving the optical properties (absorption and reduced scattering) of a reference homogeneous diffusive medium.

In the following, we first characterize the CPG fibers and discuss the tailoring of the fabrication process to increase light harvesting for use in TD-DOS. Then, we describe the experimental setup and the measurement protocol. Further, we present the performance assessment of the bioresorbable fiber system using some tests contained in the BIP and MEDPHOT protocol, as discussed above. Finally, we have challenged the use of

* Corresponding author: e-mail alberto.dallamora@polimi.it, Phone: +00 39 02 2399 6108, Fax: +00 39 02 2399 6126

bioresorbable fibers in a more realistic environment by inserting them into a cut of chicken breast, showing spectral analysis in the 500-1100 nm range. At the end, we discuss the reported results and the future perspectives.

2. Fibers fabrication and characterization

Bioresorbable phosphate glass optical fibers used in this research were manufactured by preform drawing, with the preform being obtained by the rod-in-tube technique [24,25]. We fabricated the core and cladding glasses by melting a powder batch of high purity chemicals (P_2O_5, CaO, MgO, Na_2O, B_2O_3, SiO_2) inside an alumina crucible at a temperature of around 1200 °C for 1 h under controlled atmosphere, followed by casting into preheated brass molds. We cast the core glass into a cylindrical mold to form a rod, while for the cladding glass rotational casting was carried out to obtain a tube. We then annealed both core and cladding components at a temperature around the transition temperature (T_g) for 12 h to relieve internal stresses, and finally cooled down slowly to room temperature.

We obtained the core/cladding preform by inserting the stretched core into the cladding tube and then we obtained optical fibers of different sizes (core diameters of 50, 100 and 200 µm) by drawing the preform using a drawing tower developed in-house. The furnace consists of a graphite ring heated by induction operating at 248 kHz and delivering 170 W to reach the drawing temperature (SAET, Torino, Italy).

We measured the density of the glasses at room temperature by the Archimedes' method using distilled water as immersion fluid with an estimated error of 0.005 g cm^{-3}. We performed the Differential Thermal Analysis (DTA) using a Netzsch DTA 404 PC Eos differential thermal analyzer up to 1200 °C with a heating rate of 5 °C min^{-1} in sealed Pt/Rh pans. An error of ± 3 °C was observed in measuring the characteristic temperatures. We measured the Coefficient of Thermal Expansion (CTE) with a horizontal alumina dilatometer (Netzsch, DIL 402 PC) operating at 5 °C min^{-1} on 5 mm long specimens. The measure was automatically interrupted when shrinkage higher than 0.13% was achieved. The temperature reached when the shrinkage started was defined as the softening point (T_s) of the bulk glass. CTE values were calculated in the 200-400 °C temperature range featuring an error of ± 0.1 °C^{-1}. We measured the refractive index of the glasses at five different wavelengths (633, 855, 1061, 1312, 1533 nm) through a Metricon 2010 Prism Coupler, with an estimated error of ± 0.001.

Table 1 reports the thermal properties, thermal expansion coefficient, density and refractive index of the core and cladding glasses.

The measured characteristic temperatures, T_g and T_x, indicate satisfying thermal properties of the glasses. The obtained values of the glass stability parameter $\Delta T = T_x - T_g$ are index of a good stability against crystallization of the two manufactured glasses and thus of their suitability to drawing process. From the measured refractive indexes, we obtained a Numerical Aperture (NA) of 0.17 at the wavelength of 633 nm.

Two optical fibers with core diameters of 50 and 100 µm and a rod waveguide with a core diameter of 200 µm were then drawn. The corresponding cladding diameters are 150, 300 and 600 µm. We performed optical microscopy analysis on different sections of the fibers and rod to assess their dimensions and their overall quality. Fig. 1 shows typical micrographs of the optical fiber cross-sections. No defects or bubbles are observed at the interface between core and cladding, but in some sections of the optical fiber with a core diameter of 100 µm it is possible to observe a not complete interface adhesion between core and cladding, as it can be seen in Fig. 1b.

We confirmed the guiding ability of the manufactured optical fibers by near-field images at 660 and 1300 nm, which show that the light beam is well confined inside the core of the fibers and rod.

We measured the attenuation loss of the optical fibers by cut-back method on samples of different lengths using laser diode sources operating at the edges of the first biological window (from 600 to 1300 nm). The results show attenuation loss coefficients of around 3.4 and 4.1 dB m^{-1}, measured respectively at 1300 and 633 nm. We performed optical microscopy analysis on different sections of the fibers and rod to assess their dimensions and their overall quality. Fig. 1 shows typical micrographs of the optical fiber cross-sections. No defects or bubbles are observed at the interface between core and cladding, but in some sections of the optical fiber with a core diameter of 100 µm it is possible to observe a not complete interface adhesion between core and cladding, as it can be seen in Fig. 1b.

We confirmed the guiding ability of the manufactured optical fibers by near-field images at 660 and 1300 nm, which show that the light beam is well confined inside the core of the fibers and rod.

We measured the attenuation loss of the optical fibers by cut-back method on samples of different lengths using laser diode sources operating at the edges of the first biological window (from 600 to 1300 nm). The results show attenuation loss coefficients of around 3.4 and 4.1 dB m^{-1}, measured respectively at 1300 and 633 nm.

Table 1 Glass transition temperature (T_g), crystallization temperature (T_x), glass stability parameter (ΔT), coefficient of thermal expansion (CTE), density and refractive index of the manufactured phosphate glasses.

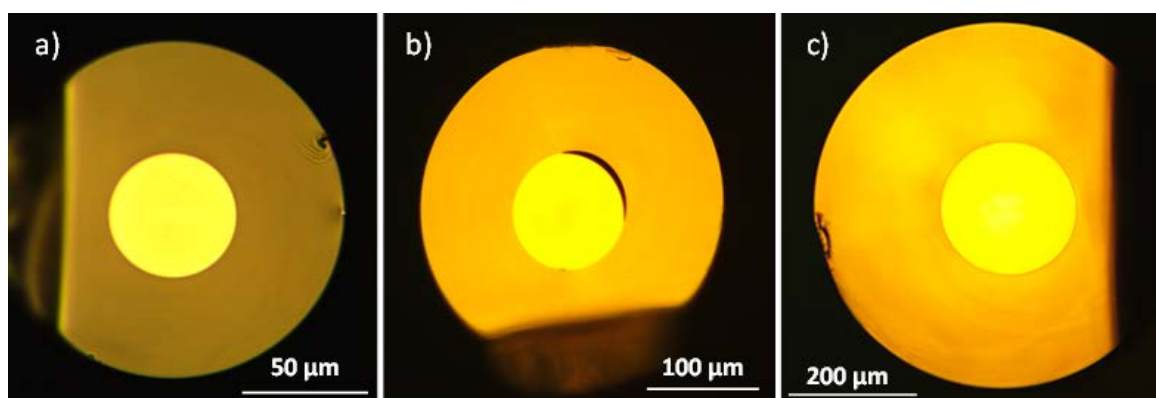|	Core	Cladding
T_g [°C] (error: ± 3°C)	446	464
T_x [°C] (error: ± 3°C)	684	611
$\Delta T = T_x - T_g$ [°C] (error: ± 6°C)	238	147
CTE [°C^{-1}] (error: ± 0.1°C^{-1})	15.3	12.2
ρ [g cm^{-3}] (error: ± 0.005 g/cm)	2.641	2.589
n @ 633 nm (error: ± 0.001)	1.529	1.519

Figure 1 Optical microscopy images of the manufactured biocompatible and resorbable phosphate glass optical fibers with different core sizes: (a) 50 μm, (b) 100 μm, (c) 200 μm.

The obtained attenuation loss values are in line with the typical values of phosphate glass optical fibers and with our previous experiments on resorbable CPG-based fibers [13,26,27] and can be mainly ascribed to the defects at the core/cladding interface of the fiber. Furthermore, these values are one up to two orders of magnitude lower in the decibel scale than those published so far for bioresorbable optical fibers, thus showing the advantage in using phosphate glass based optical waveguides for bioresorbable optics [7,9,10,14,15].

3. System setup and measurement protocol

3.1 Experimental setup

In this work, two different setups were used, depending on the purpose of the experiment. For the linearity measurements, we built a dedicated setup, while for the spectroscopic acquisition we used a setup similar to a state-of-the-art system [21]. Generally speaking, both the experimental setups were based on a pulsed laser as a light source, optical fibers for injecting and collecting the optical pulses to and from the sample, a free-running (i.e.

not time-gated) Single-Photon Avalanche Diode (SPAD) as a detector and a Time-Correlated Single-Photon Counting (TCSPC) board, as schematically depicted in Fig. 2. To send/collect light to/from the sample we used resorbable fibers (grey solid lines in Fig. 2) with different core diameters – i.e. 50, 100 and 200 μm – which were connected or spliced (depending on the core considered) to commercial glass fibers (blue solid lines). Details about the components of the setup are described below and summarized in Table 2. Compared to a state-of-the-art clinical prototype [21] operating with standard 1 mm core glass fibers with NA = 0.37, a theoretical loss in responsivity by a factor of 1900, 470, and 120 is expected assuming a large detector area (>1 mm diameter). For a small area detector, as in the case of SPADs – which offer advantages in terms of quantum efficiency, temporal resolution, noise, fast-gated capability – the effective loss is much less since not all the light harvested by a large core fiber can be coupled to the detector. In particular, for the SPAD used in this study (100 μm diameter, NA = 0.6 for the coupling optics) the theoretical losses are 50, 12 and 3 for the 50, 100, and 200 μm core fibers, respectively.

For the linearity measurements, the laser used was a four-wave mixing prototype (4WM, Fianium Ltd, UK),

providing optical pulses at 820 nm (average power ~ 90 mW, full-width half maximum – FWHM – of the pulses < 100 ps) at a rate of 40 MHz. Such a source allowed us to make use of high average optical power at a fixed wavelength, thus permitting to measure samples with absorption coefficients up to 0.70 cm^{-1} employing all the three fiber cores. For the spectroscopy measurements, we built a system close to the state-of-the-art [21], which is composed by a supercontinuum laser (SuperK Extreme, NKT Photonics, Denmark) coupled to a prism to provide optical pulses at 80 MHz with a wavelength tunable in the 500-1100 nm range. In both cases (linearity and spectroscopy measurements) the light provided by the laser source was attenuated by means of a Variable Optical Attenuator (VOA) in order to set the proper photon counting rate at the detector (i.e. ~ 700000 counts per second) to avoid distortions in TCSPC reconstructions of the distribution of photons time of flight [28]. Light is then delivered to the sample through optical fibers. The distance between injection and collection fibers (source-detector distance, ρ) was set to 20 mm and in all cases the fibers were immersed by about 30 mm into the sample so as to mimic an interstitial measurement. The photons collected by the harvesting fiber were coupled onto the detector through a doublet of lenses (see Table 2 for details). For both the linearity and the spectroscopy measurements we used a 100 μm active area diameter SPAD (Micro Photon Devices Srl, Italy).
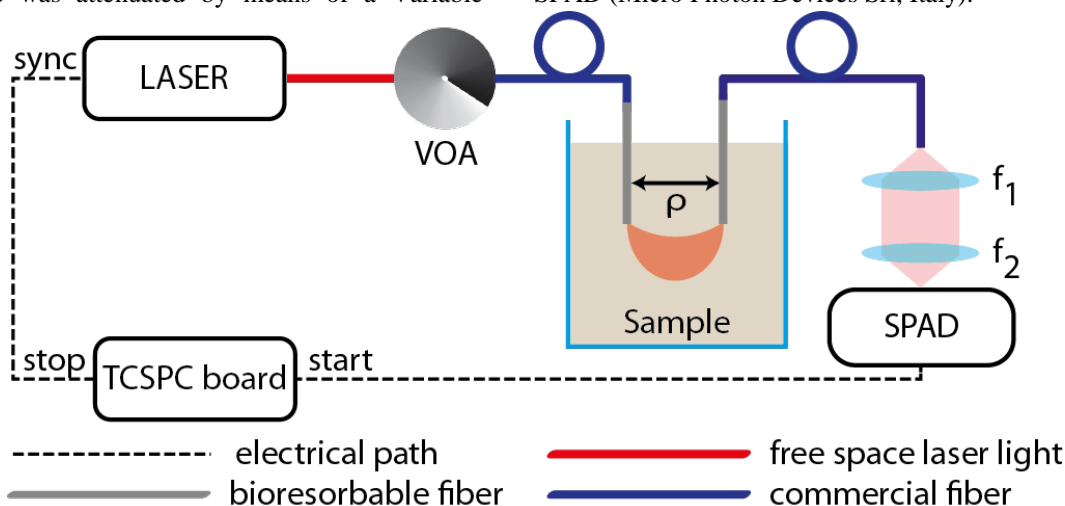

Figure 2 Schematics of the main building blocks composing the setup used for both experiments (linearity and spectroscopy measurements). Details about the main blocks can be found in Table 2.

Table 2 Details of laser sources, bioresorbable (BR) fibers and lenses used depending on the type of measurement performed.

		Linearity			Spectroscopy (similar to a state-of-the-art system [21])
Laser	Type	Four-wave mixing			Supercontinuum + prism
	Frequency	40 MHz			80 MHz
	Wavelength	820 nm			500 to 1100 nm (step: 5 nm)
	Output power	90 mW			< 3 mW
BR Fiber	Core diameter	50 μm	100 μm	200 μm	100 μm
	Numerical Aperture	0.17	0.17	0.17	0.17
	Connection to standard fibers	Splice	xyz stage	xyz stage	xyz stage
Lenses	f_1	75 mm	75 mm	75 mm	30 mm
	f_2	60 mm	60 mm	30 mm	25 mm

As depicted in Fig. 2, for both launching and collection sides each bioresorbable fiber was connected to a commercial glass fiber (Thorlabs GmbH) having the same core size. The splicing was carried out with a commercial splicer machine (Fujikura FSM-30S) for the 50 μm core fiber, while the 100 and 200 μm core fibers were coupled using 3-axis micrometric translation stages. Regardless the core sizes, the bioresorbable fibers were about 1 m long and the glass fibers coupled to the bioresorbable ones had about the same length. For linearity measurements, all fibers (50, 100 and 200 μm) were tested, while for the spectroscopy acquisition we used only the 100 μm core fiber. Table 2 summarizes the characteristics of the setup (laser, fiber used and optics) depending on the measurement that was carried out. In both setups, the synchronized signal provided by the laser in use was fed to the TCSPC board (SPC-130, Becker&Hickl GmbH, Germany) as a "stop", while the "start" signal was given by the pulse generated by the detector every time that an avalanche was triggered by a single photon.

3.2 Measurement protocol

3.2.1. Instrument Response Function

The Instrument Response Function (IRF) is one of the test assessed by the BIP protocol [22]. It characterizes the overall time resolution of the instrument as a whole and it is crucial to understand the intrinsic suitability of the developed setup for DOS measurements.

In the present implementation, the position of CPG fibers cannot be switched from the reflectance geometry

on phantoms to the transmittance geometry for the acquisition of the IRF directly facing the two fiber tips. Therefore, to acquire the IRF in reflectance geometry, we put the injection and collection fibers at a null source-detector distance and both fiber tips were in contact with the same thin layer of Teflon to provide to photons a path from the source fiber to the collection one. The use of Teflon instead of just a mirror is preferred in order to illuminate the core of the collection fiber with isotropic light to ensure to take into account the temporal mismatch between the different modes of propagation.

3.2.2. Linearity

The linearity measurement is one of the tests defined by the MEDPHOT protocol [23]. It assesses the linearity of time-domain diffuse optics instruments in retrieving the absorption and reduced scattering coefficients of a reference diffusive medium over a wide range of optical properties. Following the protocol, the linearity was checked by changing the nominal value of absorption (or scattering) coefficient of a phantom (i.e. "true" value in the following) and retrieving from the distribution of photons time of flight (as described in Section 3.3) the measured value of the absorption (or scattering) coefficient (i.e. "measured" value in the following). Therefore, taking both scattering and absorption coefficients (μ_a and μ'_s, respectively) as measurands, a total of four plots showing the measured value of absorption and reduced scattering coefficients against the true ones can be obtained.
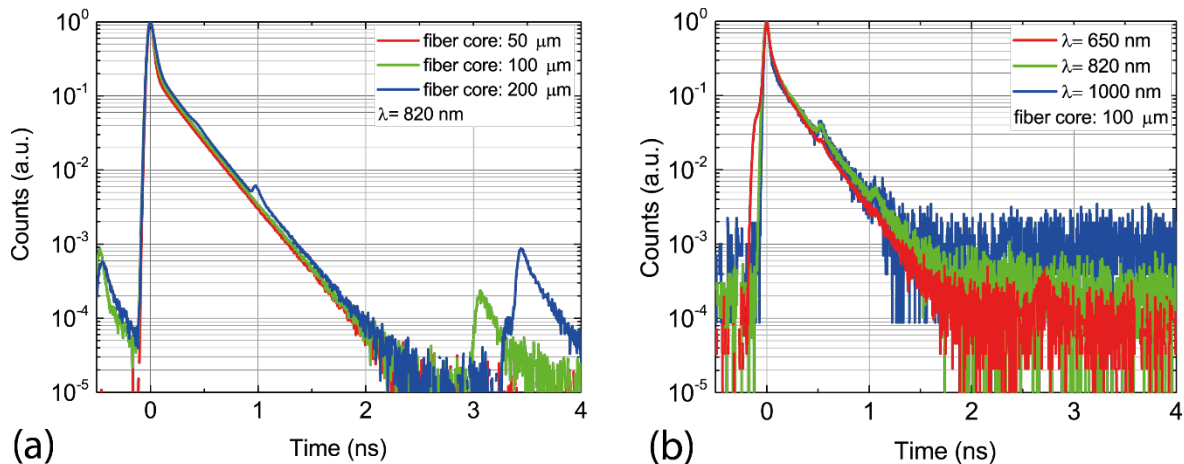

Figure 3 (a) Instrument response functions (IRFs) of the setup built for linearity measurements recorded using all fibers of the set (50, 100 and 200 μm core diameters). (b) IRFs of the setup based on the supercontinuum laser and a prism at three wavelengths (650, 820 and 1000 nm) recorded using the 100 μm core bioresorbable fiber.

For linearity measurements, we made use of a liquid phantom composed by water, Intralipid (providing scattering property) and ink (acting as absorber). The desired optical properties of the phantom can be obtained by a proper mixture of the components [29], combining 4 values for the scattering coefficient (μ_s' = 5, 10, 15 and 20 cm^{-1} at 820 nm) with 8 values for the absorption (μ_a ranging from 0.02 to about 0.70 cm^{-1}). For each scattering series, upon adding ink to the phantom, calibrated quantities of Intralipid were also added to keep the scattering constant. For each sample (with a given μ_a and μ_s') we acquired 60 measurements of 1 s each in order to increase the signal-to-noise ratio.

The same procedure was repeated for the whole set of fibers (50, 100 and 200 μm core diameters).

3.2.3. Spectroscopy

In order to demonstrate that bioresorbable fibers can be profitably used to recover the μ_a and μ_s' spectra of a living tissue, we measured the optical properties of a chicken breast. The sample (with no skin and fat) was tied in order to remove any possible air gap and to have a thickness of about 8 cm, thus avoiding border effects that can affect the fit of the acquired data. The fibers were then inserted into the sample for nearly 2.5 cm in depth and the source-detector distance was set to 20 mm. In order to compare the performances achievable using the bioresorbable fibers with those of a system close to the state-of-the-art based on standard fibers, we repeated the measurements by substituting the bioresorbable fibers with standard glass based ones (100 μm core, NA = 0.22 from Thorlabs GmbH, Germany), leaving identical the rest of the system.

The measurements were performed by tuning the laser in the range between 500 and 1100 nm at steps of 5 nm.

For each wavelength, 20 repetitions with an acquisition time of 1 s were acquired.

3.3 Data analysis

Each time-resolved curve has been used to retrieve both absorption and reduced scattering coefficients by fitting the data to an analytical model obtained under the Diffusion Approximation describing the photon transport in an infinite diffusive medium [30]:

$$\phi(r,t) = \frac{v}{(4\pi Dvt)^{3\backslash 2}} exp\left(-\frac{r^2}{4Dvt}\right) exp(-\mu_a vt) \quad (1)$$

In Eq. 1 v is the light speed in the medium, $D = 1/(3\mu_s')$ is the diffusion coefficient, t is photon travelling time and μ_a is the absorption coefficient.

The fitting algorithm is based on the minimization of the reduced χ^2 using a Levenberg-Marquardt routine [31].

The temporal broadening due to fibers and other effects is taken into account by convolving the IRF to the analytical model expressed in Eq. 1. A homogeneous semi-infinite model with extrapolated boundary conditions was used for fitting the temporal curves [30]. To increase the signal-to-noise ratio, the repetitions were summed before the analysis. The temporal range used is from 10% of the peak on the rising edge down to 1% of the peak on the falling edge of the acquired waveform.

4. Results and discussion

4.1 Instrument Response Function

Fig. 3 shows the IRFs recovered for the proposed systems after the subtraction of the constant background noise due to the dark count rate of the detector. The left picture (Fig. 3a) displays the IRFs at the wavelength of 820 nm obtained using the 4WM laser for the 3 fibers (50, 100 and 200 μm core). The FWHM is lower than 75 ps for all fibers and the dynamic range is larger than 4 decades.

The right picture (Fig. 3b) shows the IRFs for the spectroscopy setup (with 100 μm core bioresorbable fiber) after background subtraction at three wavelengths: 650, 820 and 1000 nm (randomly chosen). The dynamic range of the acquisitions is 3.5 (3 for 1000 nm) decades, while the FWHM is smaller (less than 70 ps for all the wavelengths).

For both setups and regardless the core dimension of the bioresorbable fiber used, it is clearly noticeable the presence of an exponential decay starting about one order of magnitude below the main peak. This effect is not ascribed to a behavior of the optical fibers like a fluorescence, but it is a well-known characteristic of the SPAD: the "diffusion tail" due to carriers absorbed outside the high electric field region of the silicon junction [32]. For the 100 and 200 μm core fibers (Fig. 3a), some minor peaks are present both before and after the main peak of the curve. This is most probably due to some reflections arising in the optical system (e.g. lenses to couple light onto the SPAD). Another cause could be the presence of some defects into the fibers, such as inclusions and striae [33]. These defects are often exhibited by glasses manufactured on a laboratory scale and are responsible for local fluctuations in the refractive index of the material, thus may introduce small and localized back reflections. The reflection effect is more evident in the fibers with a larger core. Indeed, for large core fibers the probability of damaging the end facets by handling during system setup is higher. For the whole fibers set and at all wavelengths, since the only exponential decay present is the diffusion tail of the SPAD, we experienced no fluorescence or backscattering from the bioresorbable fibers, which could affect

significantly the IRF and prevent the employment of the bioresorbable fibers for time-domain acquisitions.

4.2 Linearity measurements

Fig. 4 shows the results of the linearity measurements for the whole set of fibers (columns). The first row of Fig. 4 displays the linearity in absorption (measured μ_a vs. true μ_a). We can derive that the system is perfectly linear in recovering the absorption coefficient till 0.70 cm^{-1} for the 50 μm core fiber, while the 100 μm and 200 μm ones show a linear behavior till 0.37 cm^{-1}. The difference in this behavior could be due to the presence of a higher number of reflections in the larger core fibers. Such a higher number of reflections can impair the fitting procedure.

The second row of Fig. 4 shows the absorption to scattering coupling (measured μ_s' vs. true μ_a). This indicates the independency of the scattering parameter from the absorption one. For all the fibers used, we recovered nearly the same value of scattering regardless the absorption of the phantom, except for the last point at the 15 and 20 cm^{-1} scattering values, where the fit was not reliable as stated for the first row of the graph. Furthermore, some increase in scattering is observed for the higher absorption values ($\mu_a > 0.20$ cm^{-1}). This behavior is well-known in time-domain diffuse optics and it is normally attributed to an initial deviation from the diffusion approximation in the theoretical model [34]. The coupling at lower absorption for the 50 μm fiber can be explained with the fainter signal recorded (due to the lower light harvesting) that can again affect the fitting procedure. The third row of Fig. 4 shows the scattering to absorption coupling (measured μ_a vs. true μ_s'). We can notice that the coupling between absorption and scattering

is completely negligible for absorption values up to 0.37 cm^{-1} (orange line). Indeed, the absorption values recovered are always constant regardless of the scattering coefficient. As already stated, for the 100 and 200 μm fibers the points with high scattering (15 and 20 cm^{-1}) and high absorption (0.69 cm^{-1}) have an unexpected behavior. For the 50 μm fiber, there is no coupling between the measured μ_a and the true μ_s', regardless of the phantom absorption.

In the last row of Fig. 4 the linearity in scattering for all fibers is reported (measured μ_s' vs. true μ_s'). For the 50 and 100 μm core fibers, we can notice that the behavior of the system is almost linear (relative error always lower than 20%) except for the scattering values of 20 cm^{-1}. It's worth noting that for the 200 μm core fiber the linearity is well recovered for all phantoms with absorption values lower than 0.69 cm^{-1} (maximum relative error of 10.3% at $\mu_s' = 5$ cm^{-1} and $\mu_a = 0.37$ cm^{-1}, otherwise always lower than 4%).

All these measurements were performed using a laser with an average power of ∼ 90 mW so as to cover all optical properties with an acceptable number of counts ($>10^5$) and to disentangle the assessment of linearity from signal constraints – as prescribed by the MEDPHOT Protocol. For lower power sources (e.g. 1 mW average power) the poor light harvesting can surely be a problem when measuring high μ_a or high μ_s' properties.

Provided that the signal level is sufficient to perform the measurement, the good linearity behavior of the system is expected to be substantially unchanged in the whole range of wavelengths used for spectroscopy since, as proved by Fig. 3b, the IRF shows only minor changes in a broad range.
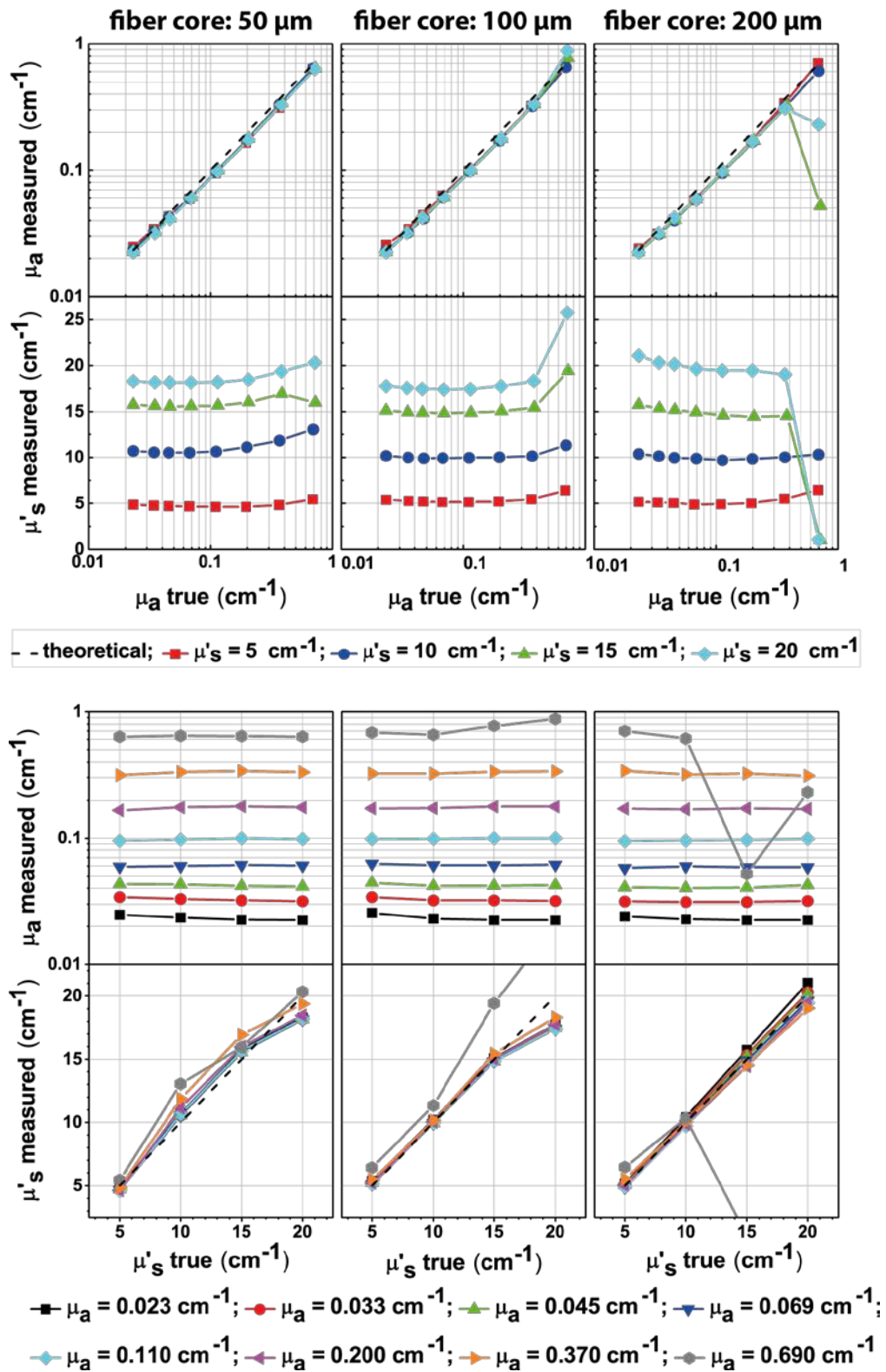
Figure 4 Results of the linearity measurements for the three sets of fibers (columns). In the first and last row, the dashed line represents the expected optical properties.
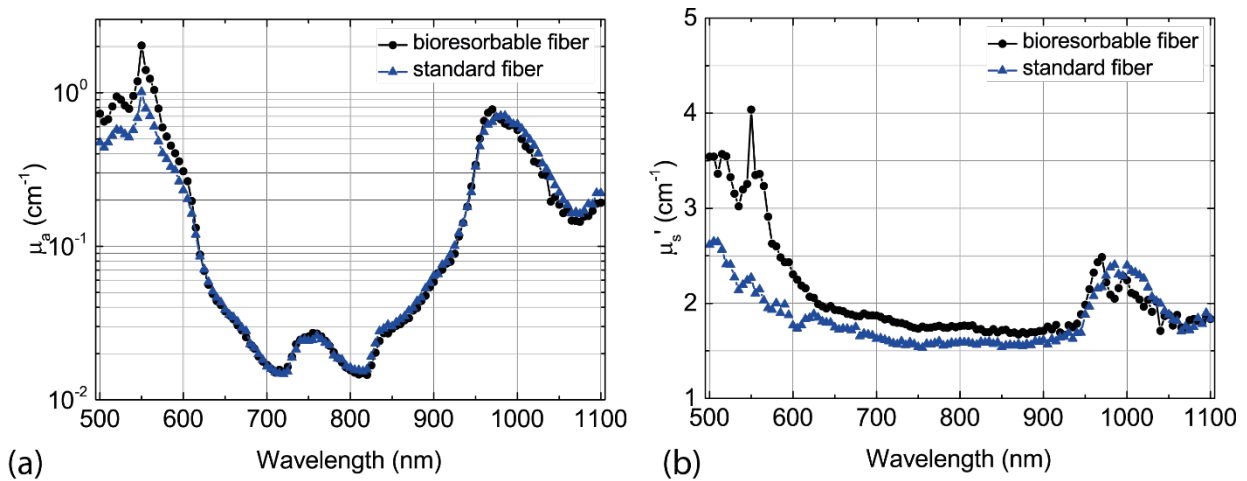
Figure 5 Recovered spectra of absorption coefficient (a) and reduced scattering (b) in a chicken breast measured using a system close to the state-of-the-art based on bioresorbable fiber (black circles) and on conventional glass fibers (blue triangles).

4.3 Spectroscopy measurements

Fig. 5a reports the recovered spectra of absorption and reduced scattering measured on a chicken breast using the 100 μm core fiber and a spectroscopic setup close to the state-of-the-art described in Section 3.1 (black circles). The spectra obtained using standard glass fibers are also shown for comparison (blue triangles). Overall, there is a fairly good overlapping of the measurements obtained with the two different fibers.

Looking at the absorption spectrum, we can clearly distinguish two main peaks: one at 550 nm and the other at 970 nm. The former is due to deoxy-hemoglobin, whose presence is also confirmed by the third broad peak at about 750 nm, while the absorption peak at 970 nm is due to the presence of water [35]. For the bioresorbable fiber, the absorption spectrum is more noisy around the water peak, while tends to be overestimated below 600 nm. In both cases we obtained a low signal using the bioresorbable fiber due to high absorption. Using a different detector (i.e. the SiPM module [36] used in a state-of-the-art system [21]) with a larger area but also higher dark count rate we observed a significant discrepancy in these two spectral regions (data not shown), thus demonstrating the need of a low noise detector to cope with the limited light harvesting of the fiber.

The retrieved scattering spectrum is low in amplitude (always lower than 3.5 cm^{-1}) and presents, except in the region around the first and third peaks, a decreasing trend with wavelength compatible with data reported in literature [35]. The low amplitude can be attributed to the chicken breast tissue, having elongated fibers that can possibly reduce the effective scattering probability. The scattering peaks, located at the same wavelengths of the absorption peaks, are caused by the absorption-to-

scattering coupling due to the failure of the diffusion approximation at high absorption and low scattering. This effect, already observed in the second row of Fig. 4, is exacerbated here because of the very low scattering. Yet, it does not prevent proper estimation of the scattering trend (related to the microstructure) that is usually assessed in the low-absorption region (e.g. 600 to 900 nm). Here the scattering spectrum follows a monotonically decreasing power law as expected from empirical derivations of Mie theory [37,38].

The spectra obtained using the two fibers are quite similar in trend, and display also the same absorption-to-scattering couplings. The bioresorbable fibers show a slightly higher scattering value (around 10%) in the "safe" 600-900 nm region. The discrepancy between the reduced scattering exhibited by the bioresorbable and conventional glass fibers reveals to be more pronounced below 600 nm, a region where low signal and absorption coupling make the scattering measurement unreliable.

5. Conclusions and future perspectives

In this paper we proposed for the first time the use of bioresorbable fibers for time-domain diffuse optics measurements. Calcium Phosphate Glass fibers (50, 100 and 200 μm core diameters) with increased numerical aperture with respect to previously reported samples were fabricated and tested in time-domain diffuse optics. Our measurements demonstrated that a system based on bioresorbable fibers is suitable for the purpose and in particular the capability of the system to properly recover optical properties of phantoms on a wide range of absorption (from 0 to 0.69 cm^{-1}) and scattering (from 5 to 20 cm^{-1}) coefficients. Additionally, we measured the

absorption and reduced scattering coefficients spectra of a chicken breast in order to obtain an ex-vivo validation of the proposed fibers. The absorption and scattering properties were found to be similar in terms of all important peaks and trends as compared to the results obtained using a system close to the state-of-the-art clinical prototype equipped with standard glass fibers.

These measurements allowed us to state that the use of bioresorbable fibers for diffuse optical spectroscopy is feasible and represents an interesting perspective for a new generation of biomedical monitoring devices since they can be implanted in the patient and follow up the evolution after a surgical intervention, without the need to remove them with additional burden.

An actual limitation is represented by the relatively low NA and small core diameter, which can reduce the overall system responsivity by orders of magnitude as compared to large core collection fibers. The core diameter cannot be increased much since flexibility and low invasiveness must be preserved. Conversely, higher NA up to an indicative value of 0.22 could be attained by properly tuning the cladding glass composition.

As a future perspective, bioresorbable fibers can be engineered to have even higher flexibility to reduce the possible generation of localized defects that can give rise to back reflections and towards potential endoscopic applications. Additionally, bioresorbable fibers can be profitably coupled with fast-gated detectors [39] to reject the peak of reflected or scarcely diffused photons that can saturate the dynamic range of a "classical" (i.e. non-gated) detector, thus allowing the use of a single interstitial fiber as already demonstrated in the case of classical optical fibers [40].

References

1.   H. Tao, J. M. Kainerstorfer, S. M. Siebert, E. M. Pritchard, A. Sassaroli, B. J. B. Panilaitis, M. A. Brenckle, J. J. Amsden, J. Levitt, S. Fantini, D. L. Kaplan, and F. G. Omenetto, "Implantable, multifunctional, bioresorbable optics," Proc. Natl. Acad. Sci. **109**, 19584–19589 (2012).

2.   M. Humar, S. J. J. Kwok, M. Choi, S. Cho, A. K. Yetisen, and S.-H. Yun, "Towards biomaterial-based implantable photonic devices," Nanophotonics **5**, 60–80 (2016).

3.   B. D. Lawrence, M. Cronin-Golomb, I. Georgakoudi, D. L. Kaplan, and F. G. Omenetto, "Bioactive Silk Protein Biomaterial Systems for Optical Devices," Biomacromolecules **9**, 1214–1220 (2008).

4.   P. Domachuk, H. Perry, J. J. Amsden, D. L. Kaplan, and F. G. Omenetto, "Bioactive "self-sensing" optical systems," Appl. Phys. Lett. **95**, 253702 (2009).

5.   E. A. Sykes, A. Albanese, and W. C. W. Chan, "Biophotonics: Implantable waveguides," Nat. Photonics **7**, 940–941 (2013).

6.   S. Nizamoglu, M. C. Gather, M. Humar, M. Choi, S. Kim, K. S. Kim, S. K. Hahn, G. Scarcelli, M. Randolph, R. W. Redmond, and S. H. Yun, "Bioabsorbable polymer optical waveguides for deep-tissue photomedicine," Nat. Commun. **7**, 10374 (2016).

7.   A. Dupuis, N. Guo, Y. Gao, N. Godbout, S. Lacroix, C. Dubois, and M. Skorobogatiy, "Prospective for biodegradable microstructured optical fibers," Opt. Lett. **32**, 109–111 (2007).

8.   N. Huby, V. Vié, A. Renault, S. Beaufils, T. Lèfevre, F. Paquet-Mercier, M. Pézolet, and B. Beche, "Native spider silk as a biological optical fiber," Appl. Phys. Lett. **102**, 123702 (2013).

9.   S. Kujala, A. Mannila, L. Karvonen, K. Kieu, and Z. Sun, "Natural Silk as a Photonics Component: a Study on Its Light Guiding and Nonlinear Optical Properties," Sci. Rep. **6**, 22358 (2016).

10.   M. Choi, J. W. Choi, S. Kim, S. Nizamoglu, S. K. Hahn, and S. H. Yun, "Light-guiding hydrogels for cell-based sensing and optogenetic synthesis in vivo," Nat. Photonics **7**, 987–994 (2013).

11.   F. Baino, G. Novajra, V. Miguez-Pacheco, A. R. Boccaccini, and C. Vitale-Brovarone, "Bioactive glasses: Special applications outside the skeletal system," J. Non. Cryst. Solids **432**, 15–30 (2016).

12.   R. M. Moss, D. M. Pickup, I. Ahmed, J. C. Knowles, M. E. Smith, and R. J. Newport, "Structural characteristics of antibacterial bioresorbable phosphate glass," Adv. Funct. Mater. **18**, 634–639 (2008).

13.   E. Ceci-Ginistrelli, D. Pugliese, N. G. Boetti, G. Novajra, A. Ambrosone, J. Lousteau, C. Vitale-Brovarone, S. Abrate, and D. Milanese, "Novel biocompatible and resorbable UV-transparent phosphate glass based optical fiber," Opt. Mater.

Express **6**, 2040–2051 (2016).

14. S. T. Parker, P. Domachuk, J. Amsden, J. Bressner, J. A. Lewis, D. L. Kaplan, and F. C. Omenetto, "Biocompatible silk printed optical waveguides," Adv. Mater. **21**, 2411–2415 (2009).

15. J. Guo, X. Liu, N. Jiang, A. K. Yetisen, H. Yuk, C. Yang, A. Khademhosseini, X. Zhao, and S.-H. Yun, "Highly Stretchable, Strain Sensing Hydrogel Optical Fibers," Adv. Mater. **28**, 10244–10249 (2016).

16. J. G. Kim and H. Liu, "Variation of haemoglobin extinction coefficients can cause errors in the determination of haemoglobin concentration measured by near-infrared spectroscopy," Phys. Med. Biol. **52**, 6295 (2007).

17. Z. Huang, "A review of progress in clinical photodynamic therapy," Technol. Cancer Res. Treat. **4**, 283–293 (2005).

18. P.-J. J. Lou, H. R. Jager, L. Jones, T. Theodossy, S. G. Bown, C. Hopper, H. R. Jäger, L. Jones, T. Theodossy, S. G. Bown, and C. Hopper, "Interstitial photodynamic therapy as salvage treatment for recurrent head and neck cancer," Br. J. Cancer **91**, 441–446 (2004).

19. T. Durduran, R. Choe, W. B. Baker, and A. G. Yodh, "Diffuse optics for tissue monitoring and tomography," Reports Prog. Phys. **73**, 76701 (2010).

20. P. Taroni, A. Bassi, D. Comelli, A. Farina, R. Cubeddu, and A. Pifferi, "Diffuse optical spectroscopy of breast tissue extended to 1100nm," J. Biomed. Opt. **14**, 54030–54037 (2009).

21. S. Konugolu Venkata Sekar, A. Dalla Mora, I. Bargigia, E. Martinenghi, C. Lindner, P. Farzam, M. Pagliazzi, T. Durduran, P. Taroni, A. Pifferi, and A. Farina, "Broadband (600-1350 nm) Time-Resolved Diffuse Optical Spectrometer for Clinical Use," IEEE J. Sel. Top. Quantum Electron. **22**, 7100609 (2016).

22. H. Wabnitz, D. R. Taubert, M. Mazurenka, O. Steinkellner, A. Jelzow, R. Macdonald, D. Milej, P. Sawosz, M. Kacprzak, A. Liebert, R. Cooper, J. Hebden, A. Pifferi, A. Farina, I. Bargigia, D. Contini, M. Caffini, L. Zucchelli, L. Spinelli, R. Cubeddu, and A. Torricelli, "Performance assessment of time-domain optical brain imagers, part 1: basic instrumental performance protocol," J. Biomed. Opt. **19**, 86010 (2014).

23. A. Pifferi, A. Torricelli, A. Bassi, P. Taroni, R. Cubeddu, H. Wabnitz, D. Grosenick, M. Möller, R. Macdonald, J. Swartling, T. Svensson, S. Andersson-Engels, R. L. P. van Veen, H. J. C. M. Sterenborg, J.-M. Tualle, H. L. Nghiem, S. Avrillier, M. Whelan, and H. Stamm, "Performance assessment of photon migration instruments: the MEDPHOT protocol," Appl. Opt. **44**, 2104–2114 (2005).

24. J. B. MacChesney, R. E. Jaeger, D. A. Pinnow, F. W. Ostermayer, T. C. Rich, and L. G. Van Uitert, "Low-loss silica core-borosilicate clad fiber optical waveguide," Appl. Phys. Lett. **23**, 340–341 (1973).

25. E. Mura, J. Lousteau, D. Milanese, S. Abrate, and V. M. Sglavo, "Phosphate glasses for optical fibers: Synthesis, characterization and mechanical properties," J. Non. Cryst. Solids **362**, 147–151 (2013).

26. Y. W. Lee, S. Sinha, M. J. F. Digonnet, R. L. Byer, and S. Jiang, "20 W single-mode Yb3+-doped phosphate fiber laser," Opt. Lett. **31**, 3255–3257 (2006).

27. N. G. Boetti, E. Ceci-Ginistrelli, D. Pugliese, G. Novajra, C. Vitale-Brovarone, J. Lousteau, S. Abrate, and D. Milanese, "Bioresorbable Calcium-Phosphate Optical Fiber," in *Advanced Photonics 2016 (IPR, NOMA, Sensors, Networks, SPPCom, SOF)* (Optical Society of America, 2016), p. JTu4A.27.

28. D. V. O' Connor and D. Phillips, *Time-Correlated Single Photon Counting* (Academic Press, 1984).

29. L. Spinelli, M. Botwicz, N. Zolek, M. Kacprzak, D. Milej, P. Sawosz, A. Liebert, U. Weigel, T. Durduran, F. Foschum, A. Kienle, F. Baribeau, S. Leclair, J.-P. Bouchard, I. Noiseux, P. Gallant, O. Mermut, A. Farina, A. Pifferi, A. Torricelli, R. Cubeddu, H.-C. Ho, M. Mazurenka, H. Wabnitz, K. Klauenberg, O. Bodnar, C. Elster, M. Bénazech-Lavoué, Y. Bérubé-Lauzière, F. Lesage, D. Khoptyar, A. A. Subash, S. Andersson-Engels, P. Di Ninni, F. Martelli, and G. Zaccanti, "Determination of reference values for optical properties of liquid phantoms based on Intralipid and India ink," Biomed. Opt. Express **5**, 2037 (2014).

30. D. Contini, F. Martelli, and G. Zaccanti, "Photon migration through a turbid slab described by a model based on diffusion approximation. I. Theory," Appl. Opt. **36**, 4587–4599 (1997).

31. W. H. Press, S. A. Teukolsky, W. T. Vetterling, and B. P. Flannery, "Numerical recipes in C," Cambridge Univ. Press **1**, 3 (1988).

32. D. Contini, A. Dalla Mora, L. Spinelli, A. Farina, A. Torricelli, R. Cubeddu, F. Martelli, G. Zaccanti, A. Tosi, G. Boso, F. Zappa, and A. Pifferi, "Effects of time-gated detection in diffuse optical imaging at short source-detector separation," J. Phys. D. Appl. Phys. **48**, 45401 (2015).

33. Schott AG, "Schott Technical Information, Optics for Devices TIE:25 "Striae in Optical Glass,"" http://www.schott.com/d/advanced_optics/21cea 63c-d62f-42b7-9161-8b7ef2d7eda5/1.0/schott_tie-25_striae_in_optical_glass_eng.pdf.

34. F. Martelli, M. Bassani, L. Alianelli, L. Zangheri, and G. Zaccanti, "Accuracy of the diffusion equation to describe photon migration through an infinite medium: numerical and experimental investigation," Phys. Med. Biol. **45**, 1359–1373 (2000).

35. S. L. Jacques, "Optical properties of biological tissues: a review," Phys. Med. Biol. **58**, R37-61 (2013).

36. E. Martinenghi, L. Di Sieno, D. Contini, M. Sanzaro, A. Pifferi, and A. Dalla Mora, "Time-resolved single-photon detection module based on silicon photomultiplier: A novel building block for time-correlated measurement systems," Rev. Sci. Instrum. **87**, 073101 (2016).

37. J. R. Mourant, T. Fuselier, J. Boyer, T. M. Johnson, and I. J. Bigio, "Predictions and measurements of scattering and absorption over broad wavelength ranges in tissue phantoms," Appl. Opt. **36**, 949–957 (1997).

38. A. M. K. Nilsson, C. Sturesson, D. L. Liu, and S. Andersson-Engels, "Changes in spectral shape of tissue optical properties in conjunction with laser-induced thermotherapy," Appl. Opt. **37**, 1256–1267 (1998).

39. A. Pifferi, A. Torricelli, L. Spinelli, D. Contini, R. Cubeddu, F. Martelli, G. Zaccanti, A. Tosi, A. Dalla Mora, F. Zappa, and S. Cova, "Time-Resolved Diffuse Reflectance Using Small Source-Detector Separation and Fast Single-Photon Gating," Phys. Rev. Lett. **100**, 138101 (2008).

40. E. Alerstam, T. Svensson, S. Andersson-Engels, L. Spinelli, D. Contini, A. Dalla Mora, A. Tosi, F. Zappa, and A. Pifferi, "Single-fiber diffuse optical time-of-flight spectroscopy," Opt. Lett. **37**, 2877–2879 (2012).